Sustainable microwave-assisted hydrothermal synthesis of carbon-supported ZrO_2 nanoparticles for H_2O_2 electrogeneration

Matheus S. Kronka[1 *], Paulo J. M. Cordeiro-Junior [1], Letícia Mira[1], Alexsandro J. dos Santos[1], Guilherme V. Fortunato[1*], Marcos R.V. Lanza[1*]

[1] *São Carlos Institute of Chemistry, University of São Paulo, Avenida Trabalhador São-Carlense 400, São Carlos, SP, 13566-590, Brazil.*

[*]Corresponding authors' e-mails:

mskonka@usp.br (M.S. Kronka)

g.fortunato@usp.br (G.V. Fortunato)

marcoslanza@usp.br (M.R.V. Lanza)

Abstract: This work proposes the use of a novel green and fast (< 1h) route for the construction of electrocatalysts by microwave-assisted hydrothermal synthesis using carbon-supported metal oxide for H_2O_2 electrogeneration. Using ZrO_2 supported on carbon black Printex L6 (PL6C) as a non-toxic model catalyst, the present study evaluated different synthesis conditions and their effects on ORR activity and selectivity via the application of the rotating ring-disk electrode (RRDE) and gas diffusion electrode (GDE) techniques. RRDE results showed that the optimized ZrO_2/PL6C catalyst presented improvements in catalytic performance of 140 mV in the $E_{1/2}$ for ORR and in selectivity for H_2O_2 production of 88.8% compared to the unmodified PL6C (78%). The improved electrocatalytic performance was attributed to the high dispersion of small ZrO_2 nanoparticles (~7 nm) in direct contact with the carbon support which helped increase the ECSA values. GDE results showed that ZrO_2/PL6C was responsible for doubling the k_{app} values of H_2O_2 production and for the reduction of energy consumption by about 150 kWh g^{-1} compared to the unmodified matrix. Key insights related to the construction of carbon-based metal oxide catalysts and the optimization of ORR are discussed further in the work aiming at providing useful contributions for future investigations and applications.

Keywords: Oxygen reduction reaction, hydrogen peroxide, gas diffusion electrode, zirconium oxide nanoparticle, carbon black. microwave-assisted hydrothermal synthesis.

1. Introduction

Hydrogen peroxide (H_2O_2) is a versatile oxidizer which is widely employed for industrial, commercial, and domestic purposes [1,2]. Considered a green oxidizer, H_2O_2 has also been intensively applied in the environmental area [3–5]. Commercial H_2O_2 is mostly produced by the conventional method based on the oxidation of anthraquinone; this mechanism has been subject to criticism due to the environmental, logistic, and safety problems involved in this conventional process of H_2O_2 production [6–8]. For small scale and on-site applications, such as in the case of water treatment which typically requires low concentrations (<0.1 wt.%), the use of decentralized or *in situ* methods of H_2O_2 production has been found to help effectively overcome the risks involving the transport, storage, and dilution of H_2O_2 presented by the conventional method [3]. The electrosynthesis of H_2O_2 via oxygen reduction reaction (ORR) has drawn considerable attention as a decentralized and environmentally friendly mechanism for H_2O_2 production [4]. However, due to the slow kinetics of ORR and the possibility of leading to the production of H_2O instead of H_2O_2, the successful implementation of H_2O_2 electrosynthesis still depends on the development of economically viable materials that are able to catalyze ORR in an efficiently selective manner [4,9–11].

Platinum (Pt) and Palladium (Pd) are regarded the most active materials for ORR; however, due to their strong interaction with oxygen and oxygenated intermediates, these materials tend to break the O=O bonding mechanism, and this gives rise to the production of H_2O as the main product of reaction in a 4-electron pathway ($O_2 + 4H^+ + 4e^- \rightarrow 2H_2O$) [12,13]. In contrast, Au, Ag, Hg or C-based materials are found to be less active and tend to reduce O_2 to H_2O_2 via a 2-electron reaction pathway ($O_2 + 2H^+ + 2e^- \rightarrow H_2O_2$) as a result of their weaker interaction with oxygen [6,13–15]. Different synthesis strategies have been investigated with a view to blending the high activity of Pt and Pd with the high

selectivity demonstrated by Au, Ag, Hg, and C [16–20]. However, the scarcity and high costs of these materials make real large-scale applications of noble metal-based catalysts unfeasible. As an alternative, several studies published in the literature have investigated the functionalization or modification of carbonaceous materials with a view toward improving their catalytic performance [8,21,22]. The fact that carbon materials, such as carbon black, are cheap to obtain, they are economically viable to be employed as catalysts when it comes to large-scale applications; furthermore, these materials have been shown to exhibit high selectivity toward H_2O_2 production [8–10,18,23–27]. On the other hand, unmodified carbon-based materials have been found to present low ORR activity in acidic medium; as such, they have been found to consume high amount of energy in the H_2O_2 production process [9,10,18,23–26,28,29].

Several noble metal-free modifiers for carbon matrices have been intensively investigated aiming at enhancing their ORR activity and selectivity, as well as their electrochemical stability in acidic medium [29–35]. Carbon modification through the application of low loadings of metal oxides, such as ZrO_2 (1 - 5 wt. %) on graphene [36] or carbon black [37], Nb_2O_5 (15 wt. %) on carbon black L6 [32], V_2O_5 (7 wt. %) on Vulcan XC, and CeO_2 (2-25 wt. %) on different carbonaceous matrices [38–41], has been found to promote synergistic effects which help improve ORR activity and selectivity of the carbon-modified materials used in H_2O_2 production. In the absence of a general consensus on the issue, studies published in the literature regarding the use of carbon-modified materials have attributed the improvement in ORR activity and selectivity to several factors including increased active area, wettability of the electronic surface, and the oxophilic character of the chemical species.

Although the thermal method is the most common route for the production of metal oxides [37,41,42], the typical application of high temperature (over than 500 ºC) required

in this method limits its use for the synthesis of carbon-supported metal oxides due to the carbon oxidation process involved. As an alternative, hydrothermal routes have gained considerable popularity among researchers in the field; this technique is conducted with low toxicity solvent and requires relatively lower temperature conditions (<200 ºC). The water at high pressure and temperature presents low viscosity, and this contributes to an increase in the solubility of ionic species, leading to the rapid formation of oxide nuclei [32,36,43,44]. Advances in the hydrothermal technique have given rise to the microwave-assisted approach where microwave is used as a source of energy. The microwave-assisted hydrothermal synthesis method (MAH) can be considered an energy-saving and environmentally green method due to three factors: 1) fast production of oxides (10-60 minutes); 2) homogeneous heating without loss by dissipation; and 3) the use of water as solvent [45–48].

In this work, we propose the use of a novel, green and fast (< 1h) microwave-assisted hydrothermal synthesis route for the production of functionalized carbon-supported metal oxide catalysts employed in the electrosynthesis of H_2O_2. Based on the use of zirconium oxide supported on carbon black Printex L6 as a non-toxic (in comparison with other transition metals) [49] model catalyst for ORR, the study sought to optimize the synthesis conditions by varying the synthesis parameters (including metal precursor concentration, synthesis time, temperature, and pressure) and investigating the effects of these parameters on the ORR activity and selectivity via the use of the rotating ring-disk electrode technique. The use of the optimized catalysts resulted in greater H_2O_2 electrogeneration, which was validated by the gas-diffusion electrode technique. Key insights related to the construction of the carbon-supported metal oxide catalysts are presented as well as novel contributions for future investigations and applications.

2. Experimental

2.1 Chemicals

All reagents used for conducting the experiments were of analytical grade and were used as received. The reagents employed included the following: metallic precursor salt $(ZrO_2)_2CO_2.H_2O$ (Alfa Aesar), Printex L6 pigment carbon (PL6C, Evonik do Brasil Ltda), sulfuric acid (Vetec, 97.8%), isopropyl alcohol (Vetec, 99.5%), potassium sulfate (Sigma-Aldrich, 99%), potassium hydroxide (J. T. Baker, 99%) and 60% w/w poly(tetrafluoroethylene) (PTFE) dispersion (Uniflon). All solutions were prepared using ultrapure water from a Milli-Q system with resistivity >18 MΩ cm and temperature of 25 ^{o}C.

2.2 Microwave-assisted hydrothermal synthesis (MAH)

The MAH method proposed by Moreira et al. [46] was adapted in order to incorporate ZrO_2 on carbon black electrode support (PL6C). Initially, an amount of 0.180 g of the metal precursor $(ZrO_2)_2CO_2.H_2O$ was dissolved in a minimum amount of HNO_3 (10 mL) under sonic stirring. Afterwards, 1.0 g of Printex L6 carbon and 11.0 g of KOH, which yielded an oxidizing medium of 2 mol L^{-1} in a total volume solution of 100 mL, were added to the solution; the solution was then kept under mechanical stirring for 20 minutes. The mixture was subsequently placed in a 140 mL Teflon reactor, making sure that 80 % of its volumetric capacity was used before it was placed in the microwave for the hydrothermal reaction to occur.

The MAH procedure was optimized by varying the synthesis parameters: the percentages of the metal precursor Zr employed were 5, 10 and 15 wt.% in relation to the quantity of PL6C; the periods of synthesis applied were 10, 20, 40, 60, and 120 minutes; and the temperature levels of 120, 140 and 160 ^{o}C, with 2, 4 and 7 atm of pressure, respectively, were used. The microwave oven used for the synthesis of ZrO_2 was adapted

from the Panasonic® commercial device, model NN-ST354WRU, of 25 L and operated at maximum power of 800 W. The microwave reactor was made of Teflon and was hermetically sealed; this meant that temperatures above the boiling point of solvents could be applied on the equipment, modifying the pressure of the system. The synthesized material was washed by centrifugation with ultrapure water at least 5 times and then left to dry overnight at 80 ºC.

2.3 Electrochemical studies of ORR

Electrochemical assays were performed in a rotating ring-disk electrode (RRDE) via the application of the porous microlayer technique on the disk electrode. The RRDE tip was composed of a glassy carbon (GC) disk and Pt ring (efficiency collection (*N*) = 0.37), acquired from Pine Instrumentation. A microlayer of the catalyst with loading of 200 μg cm^{-2} was formed on the GC disk (geometric area = 0.2475 cm^2) by drop-casting 25 μL of a solution previously prepared from 2 mg of the catalyst powder, 0.5 mL of water, and 0.5 mL of isopropanol.

The electrochemical measurements were performed using a bi-potentiostat PGSTAT 128N from Metrohm AUTOLAB coupled to a rotation module - PINE model AFMSRCE. The cyclic voltammetry (CV) analyses were performed in the potential range of -0.8 to 1.0 $V_{Ag/AgCl}$ and scan rate of 50 mVs^{-1}. The ORR was studied by linear sweep voltammetry (LSV) in the range of 0.4 to -0.8 $V_{Ag/AgCl,}$ at scan rate of 5 mVs^{-1} and rotating speed of 900 rpm. The CVs and LSVs were performed in both N_2- and O_2-saturated 0.1 mol L^{-1} K_2SO_4 (pH 2.5) used as electrolyte.

The electrochemically active surface area (*ECSA*) values were determined by the double-layer capacitance (C_{dl}) method based on the work of Jaramillo [50]. To estimate these values, CVs were obtained at several scan rates (5, 20, 50, 100, and 200 mV s^{-1}) starting from the more positive to negative direction in N_2-saturated 0.1 mol L^{-1} K_2SO_4 at

pH 2.5 in 0.1 V potential range centered at the open-circuit potential (OCP). The working electrode was kept for 10 seconds at each vertex potential at the beginning of each scan. The capacitance values were calculated as follows:

$$C_{dl} = \left(\left(\frac{\Delta I}{2}\right) = \left(\frac{I_a - I_c}{2}\right)\right)/\upsilon \quad (1)$$

where I_a and I_c are the anodic and cathodic currents at the OCP, and υ is the potential scan rate. *ECSA* values were obtained by dividing the C_{dl} values by the specific capacitance (C_s) of the solution (17 µF cm^{-2}) [50].

2.4 Materials characterization

The loading of ZrO_2 was determined by thermogravimetry analysis using a TGA-50 thermogravimetric analyzer (Shimadzu). The samples (~5 mg) were burned under a synthetic air 5.0 FID gas flow (50 mL min^{-1}) at temperatures ranging between 25 and 900 ^oC, at a heating rate of 10 ^oC min^{-1}. The X-ray fluorescence (XRF) technique was used for the conduct of qualitative analyses aimed at determining the loading of ZrO_2. The XRF analysis was performed using an X-ray fluorescence spectrometer - PANalytical - Model: MiniPaI4.

The morphological characterization of the catalysts was performed by scanning electron microscopy (SEM) and transmission electron microscopy (TEM). The SEM analysis was conducted using the Jeol JSM 7500F model microscope. The TEM analysis was conducted using FEI TECNAI G^2 F20 HRTEM microscope, operating at 200 kV. The TEM samples were prepared by dripping the catalyst solution onto a 300-mesh copper TEM grid (Electron Microscopy Sciences).

The structural analysis of the catalysts was conducted by X-ray diffraction (XRD) using a Bruker X-ray diffractometer model D8 Advance, which was operated under the following conditions: 40 kV and 40 mA (1.6 kW), Cu-Kα radiation (λ = 1.540501 Å/8,047 keV), scanning rate of 0.02° s^{-1} in 2θ, with Si powder used as reference.

The surface chemistry of the catalysts was analyzed by X-ray photoelectron spectroscopy (XPS) using Scienta Omicron ESCA+ spectrometer Al Kα line (energy = 1486.6 eV) as excitation source at 20 kV with 25 W. The binding energies of the survey spectra were calibrated based on the C 1s signal at 284.6 eV. The inelastic background of the high-resolution spectra was subtracted by the Shirley method. The Voigt-type function, with Gaussian and Lorentzian combinations (in the proportion of 70:30), was used for the deconvolution of Zr 3d, C 1s and O 1s regions.

2.5 Accumulation of H_2O_2 in the bench-scale electrochemical cell

The analysis of the electrogeneration and accumulation of H_2O_2 was performed using the gas-diffusion electrode (GDE) technique. The assays were carried out in a bench-scale electrochemical cell with 3 electrodes, which consisted of a GDE used as the working cathode electrode, a platinized titanium plate used as counter electrode, and Ag/AgCl (3 mol L^{-1}, Analyser Co) used as reference electrode. The GDE cathode was produced based on the adaptation of the work of Valim et al. [31] (see details in Supplementary Information). The electrolysis assays used for the production of H_2O_2 were performed potentiostatically with the aid of the PGSTAT 128 equipment - from Metrohm AUTOLAB, coupled to a booster current module (BSTR-10A). A cell volume of 250 mL and 0.1 mol L^{-1} K_2SO_4 (used as electrolyte) at pH= 2.5 (adjusted with sulfuric acid) were used in all the experiments.

The quantification of H_2O_2 was performed by the photometric method through the complexation of 0.5 mL H_2O_2 with 4.0 mL $(NH_4)_6Mo_7O_{24}$ solution using UV-1900 spectrophotometer (acquired from Shimadzu). Under this method, hydrogen peroxide reacts with molybdate, generating a yellowish stable complex (peroxymolybdate) which is quantified by UV-Vis spectrophotometry at wavelength = 350 nm [51,52]. The C_{H2O2} values were used for calculating the energy consumption (EC) based on Eq. 2 below:

$$EC\ (kWh\ kg^{-1}) = \frac{1000\ E_{cell}\ I\ t}{V_S\ C_{H2O2}} \quad (2)$$

where E_{cell} is the potential of the electrochemical cell (in V), I is the current for each potential applied (in A), t is the time of electrolysis (in h), and V_s is the volume of the solution (in L).

3. Results and discussion

3.1 Effect of initial Zr precursor concentration

Figure 1a presents a schematic illustration of the stages involving the MAH synthesis method. Further features of MAH synthesis and advances over conventional hydrothermal methodology are detailed in the supplementary material. Thus, initially, the zirconium precursor concentration was varied between 5 to 15 wt.%, while the temperature, pH, and MAH reaction time were fixed at 140 ºC, 12, and 40 minutes, respectively. The effects of these changes in parameter conditions on the structure, morphology, and metal oxide loading are shown in Figure 1b-g.

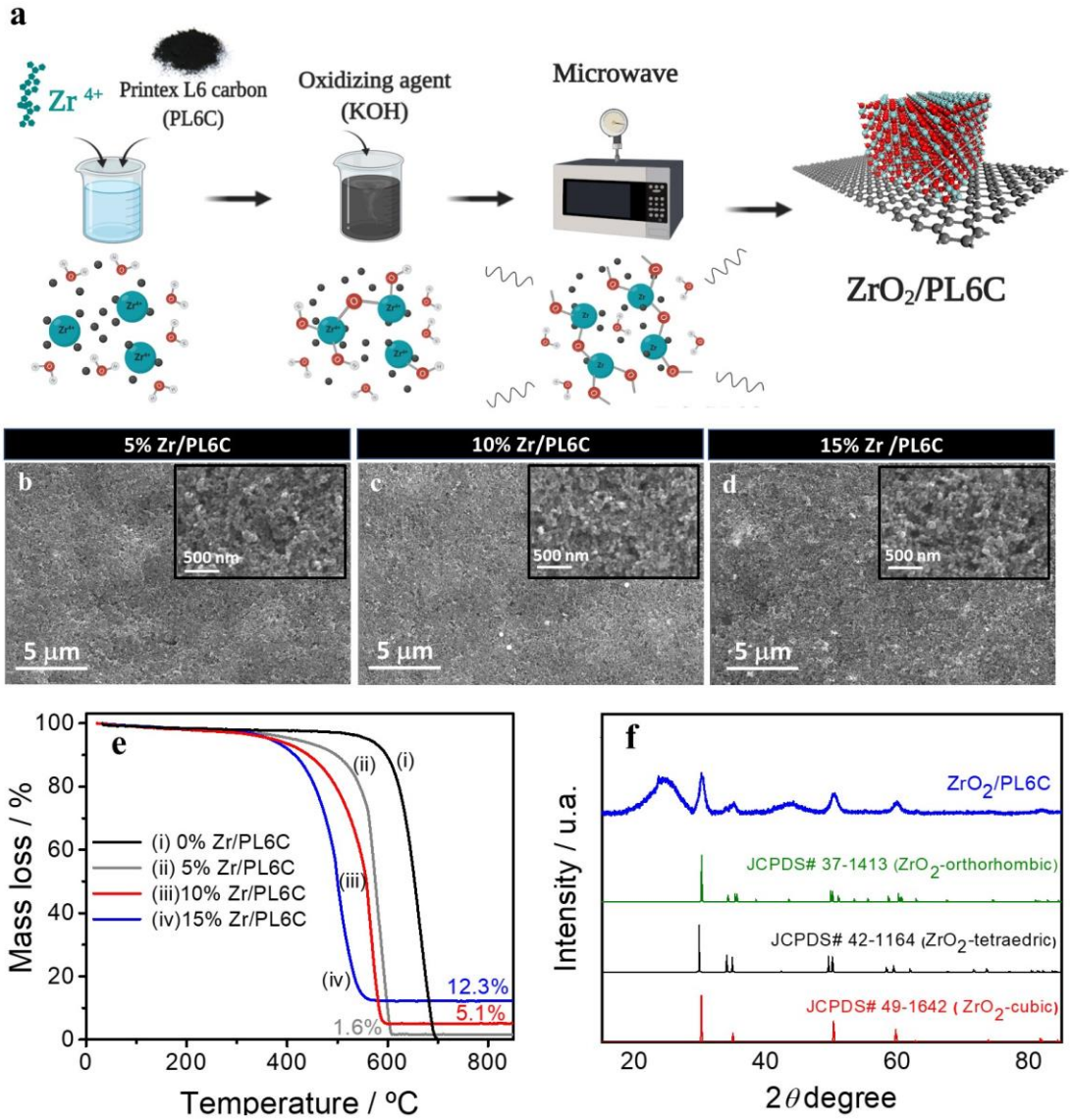

Figure 1. (a) An illustrative scheme of the microwave-assisted hydrothermal synthesis. SEM images of (b) 5, (c) 10 and (d) 15wt.% of ZrO_2/PL6C; (e) thermogravimetric analysis of the ZrO_2/PL6C catalyst produced from the application of different initial Zr precursor concentrations; (f) XRD pattern for ZrO_2/PL6C catalyst produced from the initial Zr precursor concentration of 15 wt.%.

The SEM images (Figs. 1b-d) show the successful incorporation and the morphologies of ZrO_2 nanoparticles supported on PL6C. Small ZrO_2 nanoparticles (NPs) can be found widely dispersed on the carbon support; this implies the occurrence of a high interaction between the metal oxide and the carbon support. The TEM images (Fig. S1) clearly show that the ZrO_2 NPs, characterized by an almost spherical shape, are in direct contact with the PL6C. These images also suggest the formation of agglomerates in some

regions. The SEM images obtained in back-scattered electron (BSE) imaging mode (Figs. S2) point to an increase in the loading of ZrO_2 with higher initial concentrations of the zirconium precursor. The MAH process conducted using concentrations above Zr-5 wt.% Zr led to the formation of large porous agglomerates (c.f. Fig. S1), which reached up to ~1 μm (at 15 wt.% of Zr).

The EDX spectra (Fig. S3) for 15 wt.% Zr/PL6C and control PL6C matrix (with 0 wt.% of Zr) show the presence of Zr (as the main metal in the composition), in addition to carbon and oxygen which belong to the carbonaceous material. SEM images in BSE mode (Fig. S3) for control PL6C matrix (with 0 wt.% of Zr) and PL6C with 15% wt. of Zr evinced the incorporation of ZrO_2 oxides by the MAH method. The negligible presence of potassium can be attributed to the KOH residues from the synthesis procedure. The results obtained from the thermogravimetric analyses (Fig. 1e) showed that, for the synthesis conducted using 5, 10, and 15 wt.% of Zr, only 1.6, 5.1, and 12.3 wt.% of Zr loading, respectively, were effectively incorporated into the catalysts. The use of higher initial concentrations of Zr (10 and 15 wt.%) contributed toward greater efficiency in the incorporation of the metal oxide nanoparticles; this can be attributed to the agglomeration of particles (c.f. Figs. 1, S1 and S2), which is fueled by the absence of surfactant or other structuring agent during the synthesis process. The adsorbed oxygenated anions (i.e. hydroxyl and carbonate) and the small Zr particles formed previously act as a favorable anchor point for the Zr ions available in the solution to be crystallized rather than to produce new clusters on the PL6C [53].

The results obtained from the crystallographic analysis by X-ray diffraction for the 15 wt.% Zr/PL6C sample (Fig. 1f) showed the presence of four major broadened diffraction peaks at 2Θ = 30.1°, 34.9°, 50.3°, and 59.9° which corresponded to the following crystalline planes: (1 1 1), (2 0 0), (2 2 0) and (3 1 1), respectively. This XRD

pattern can be associated to an overlapping of the peaks related to cubic, orthorhombic, and tetragonal crystalline features; the pattern indicated that the ZrO_2 nanoparticles were formed by a mix of these three crystal phases [37,54,55]. Also, the peak at 25.9° was found to be related to the plane (0 0 2) which corresponded to graphitic structures that are typically present in carbon materials [32,37,56]. The result obtained from the XRD analysis was found to be in line with other previously reported results obtained for ZrO_2 structures [37].

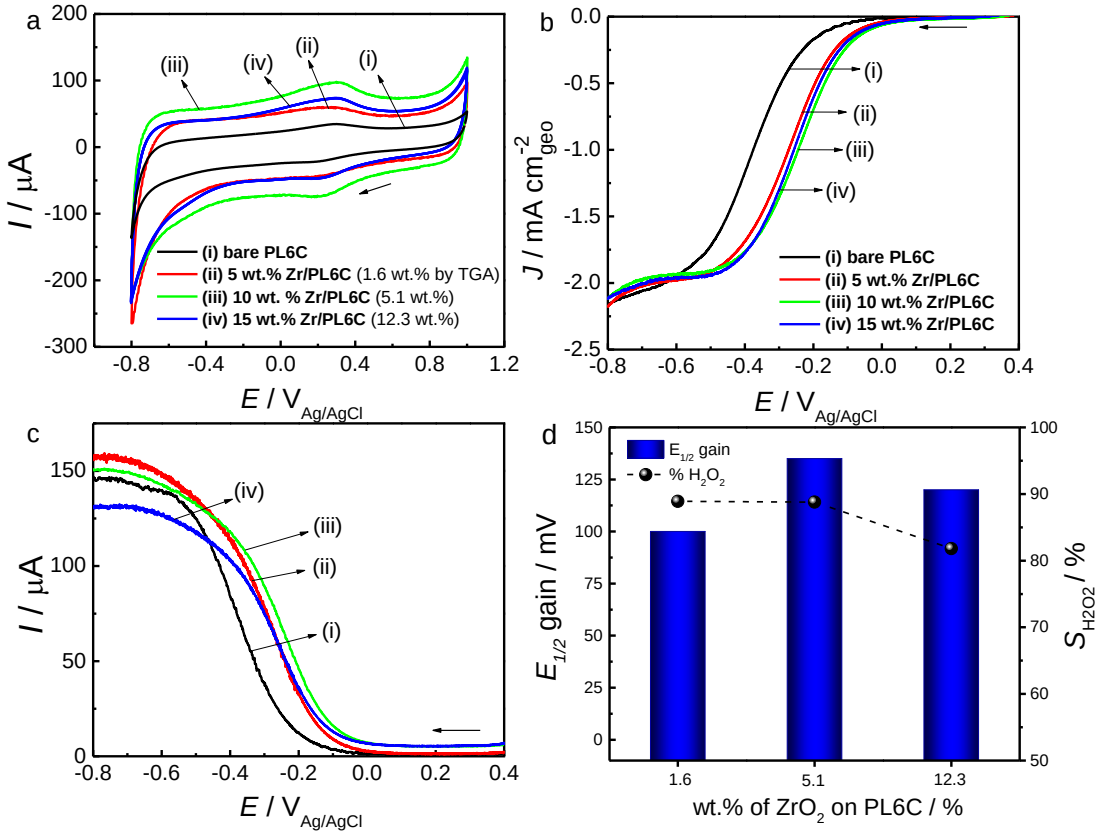

Figure 2. (a) Cyclic voltammograms obtained from the application of N_2-saturated 0.1 mol L^{-1} K_2SO_4, with pH=2.5 (H_2SO_4 adjusted), at scan rate of 50 mV s^{-1} and potential window ranging from 1 to -0.8 $V_{Ag/AgCl}$. **(b)** Linear sweep voltammetry in RRDE curves for the disk electrode obtained in O_2-saturated 0.1 mol L^{-1} K_2SO_4, with pH=2.5 (H_2SO_4 adjusted), at scan rate of 5 mV^{-1} and potential window ranging from 0.4 to -0.8 V at 900 rpm. **(c)** The values of the currents obtained for the Pt ring electrode during the potential scan on the disk electrode. The ring potential was kept at 1.0 $V_{Ag/AgCl}$. (d) Correlation between improvement in catalytic performance (in terms of $E_{1/2}$), selectivity for H_2O_2 (S_{H2O2}), and wt.% of ZrO_2 on PL6C.

Figure 2 shows the electrochemical characterization and the assessment of ORR activity and selectivity toward the production of H_2O_2 for the materials synthesized under the MAH method. The voltammetric profiles (Fig. 2a) showed the predominance of the capacitive characteristic typical for carbonaceous materials with high surface area for all the curves. One can notice the presence of a redox couple peaks centered at ~0.3 $V_{Ag/AgCl}$ which corresponded to the quinone groups of the PL6C matrix [30,57,58]. As expected, no peaks related to the ZrO_2 species were detected in the CV profiles. Nonetheless, an increase in current was observed in the presence of ZrO_2; this was attributed to the highly porous structure of ZrO_2, as observed in the TEM images (Fig. S1), which led to an increase in the surface area of the catalyst. In fact, the result obtained from the determination of the electrochemically active surface area (*ECSA*) by the capacitance method (c.f. Fig. S4 and Table S1) showed a significant increase in the *ECSA* value from 85.6 $m^2\ g^{-1}$, for the unmodified PL6C, to 128.2 $m^2\ g^{-1}$, for the modified 5.1 wt.% ZrO_2-PL6C.

The LSV curves presented in Figure 2b show the ORR electrocatalytic performance of the catalysts synthesized in this work. One can observe that all the samples modified with ZrO_2 exhibited a relatively higher ORR activity compared to the unmodified PL6C. This higher ORR activity was evidenced by the shift of the curves to more positive potentials, which was reflected in the average catalytic improvement of 115 mV in the half-wave potential ($E_{1/2}$) following the modification of the carbon matrix with ZrO_2. To find out whether H_2O_2 was eventually formed during the ORR, the Pt ring electrode was kept fixed at 1.0 V; this is regarded a favorable potential for the oxidization of H_2O_2. The LSV curves obtained for th Pt ring electrode are shown in Figure 2c. The LSV curves related to the ring confirm that, despite slight variations in the currents, all

the materials exhibited high selectivity for H_2O_2 generation. Based on the data related to the disk, the ring currents and Eq. 3 below - proposed by Paulus et al. [59], we were able to estimate the selectivity of the material with respect to H_2O_2 generation (S_{H2O2}) during the ORR.

$$S_{H2O2} = \frac{2\, i_r/N}{i_d + i_r/N}\, 100\% \qquad (3)$$

where i_d is the current of the disk, i_r is the ring current, and N is the collection number for the ring electrode (N=0.37, as provided by the manufacturer of the RRDE system).

Figure 3d shows the relation between the loading of ZrO_2 on the carbon support and its effect on the ORR activity, in terms of half-wave potential ($E_{1/2}$), and on selectivity toward H_2O_2 production (S_{H2O2}). The results obtained showed that the incorporation of ZrO_2 on the PL6C led to an increase in ORR activity and the initial selectivity of PL6C was found to be over 85%. The material derived from the application of 10 wt.% of Zr on PL6C, which effectively led to the incorporation of 5.1 wt.% of ZrO_2 on the carbon matrix, exhibited the best catalytic performance with 88% of S_{H2O2} and an improvement in catalytic performance of ~140 mV (in the $E_{1/2}$). The improvement observed in the electrocatalytic performance can be attributed to the following factors: 1) the presence of highly dispersed small particles on PL6C; and 2) the increase in *ECSA*, which helped improve the access to the catalyst surface [60] (one cannot rule out the influence of the oxophilic character of ZrO_2 [61] - its ability to dislocate the electrons from PL6C, which may influence ORR activity on the carbon surface).

However, one needs to point out that an increase in the ZrO_2 loading led to a slight decrease in both $E_{1/2}$ and $S_{H2O2;}$ this is likely due to the increase in the surface resistivity and the formation of large agglomerates [60]. Studies published in the literature suggest that given that the metal oxide has typically low conductivity, the small particles, which are in direct contact with the highly conductive carbon support, are the only particles that

can effectively participate in the ORR [60]. Thus, striking a balance between the dispersion of the particles, the *ECSA*, and the oxide loading is key to improving the ORR catalytic activity of carbon materials via modification with metal oxide.

3.2 Effect of microwave-assisted hydrothermal synthesis time

After determining the optimal concentration of the metal precursor (at 10 wt.% of Zr) of the assessed percentages, the microwave-assisted hydrothermal synthesis time was the second relevant synthesis parameter that needed to be evaluated. Microwave-assisted hydrothermal synthesis was performed in 10, 20, 40, 60 and 120 min aiming at producing ZrO_2 crystallites on the carbonaceous matrix; the changes in the material structure were monitored by SEM, TEM, and XRF analyses, as shown in Figure 3.

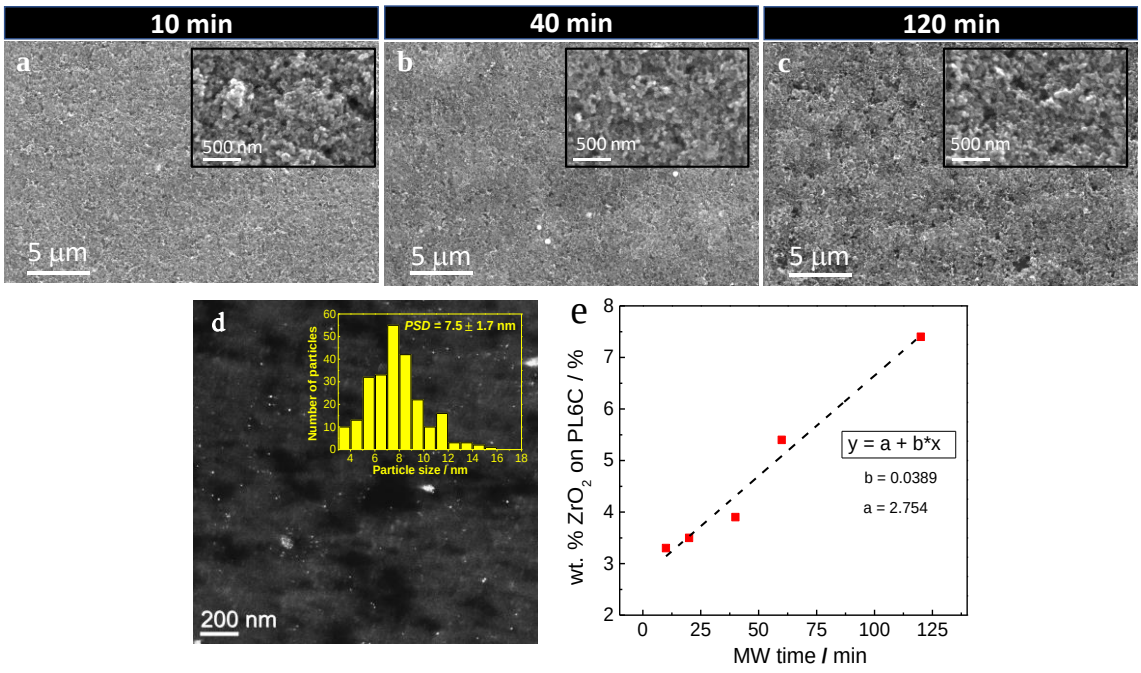

Figure 3. SEM images in SE mode for the ZrO_2/PL6C catalyst produced under different MAH synthesis in (a) 10, (b) 40 and (c) 120 minutes. (d) Dark-field STEM image and particle size distribution (inset) for the ZrO_2/PL6C sample produced in 40 min. (e) ZrO_2 wt.% on carbon *vs.* MAH time plot. Data obtained by XRF quantification.

SEM images presented in Figures 3a-c show that the duration time of the MAH synthesis plays an influential role on the nucleation-growth process. Although all the samples presented very similar structures, the SEM images on BSE mode (see Fig. S5) showed an increase in the number and size of ZrO_2 particles crystallized on PL6C as the synthesis time was increased. For illustrative purposes, the dark-field STEM image (Fig. 3d) obtained for the catalyst treated for 40 min under the MAH synthesis method shows a wide distribution of small ZrO_2 nanoparticles with average size of 7.5±1.7 nm (c.f. inset in Fig. 3d) on the carbon matrix and a formation of few agglomerates of particles. As expected, the XRF quantification (Fig. 3e) analysis indicates that the duration time of the MAH synthesis process directly influences the loading of the metal oxide crystallized on the carbon matrix. The analysis of the slope of ZrO_2 wt.% *vs.* synthesis time plot shows that the oxide crystallization process has a relatively slow kinetics (deposition rate ~ 0.04 $wt.\%_{ZrO2/C}\ min^{-1}$); in addition to that, the synthesis time needs to be greater than 3 h for all the Zr^{4+} available in the reaction media (10 wt. %) to be theoretically crystallized.

Figure 4a shows the voltammetric profiles for the catalysts produced under different synthesis times. One will notice that, for all the synthesis times investigated, the presence of ZrO_2 led to an increase in the capacitive currents of the modified PL6C in comparison to the unmodified PL6C. However, the application of periods of time longer than 40 min led to a slight decrease in the capacitive currents, which can be attributed to the formation of large oxide particles and a consequent decrease in the surface area. These voltammetric responses are in good agreement with the SEM and TEM images shown in Figs. 3a-d and S5.

Figure 4b shows the results obtained from the analysis of ORR activity. The LSV curves related to the disk electrode (Figs. 4b) show the enhancement of the ORR activity as the synthesis time is increased up to 40 min. In longer synthesis times above

40 min, the improvement in ORR activity is found to stabilize while a slight decrease in ring currents is observed (Fig. 4c). The correlation between the improvement in catalytic performance (in terms of $E_{1/2}$), selectivity toward H_2O_2 (S_{H2O2}), and MAH synthesis time (Figure 4d) shows that the ZrO_2/PL6C catalyst produced in the synthesis time of 40 min exhibits the highest ORR activity with $E_{1/2}$ improvement of ~135 mV and the highest selectivity for H_2O_2 generation (88%). These results help confirm the hypothesis that an increase in ZrO_2 loading on the carbon matrix leads to an increase in surface resistivity due to the formation of large agglomerates of oxide particles that are in poor contact with the conductive carbon support and which effectively do not take part in the reaction.

To investigate whether the synthesis procedure caused changes in the catalytic properties for ORR of bare PL6C, the control carbon matrix (with 0 wt.% of Zr) was subjected to the same synthesis conditions in the absence of the metal precursor. Interestingly, even after the control material has been exposed to high pressure in a highly alkaline condition, the RRDE results (c.f. Fig. S6) showed no substantial changes in the electrocatalytic behavior for ORR.

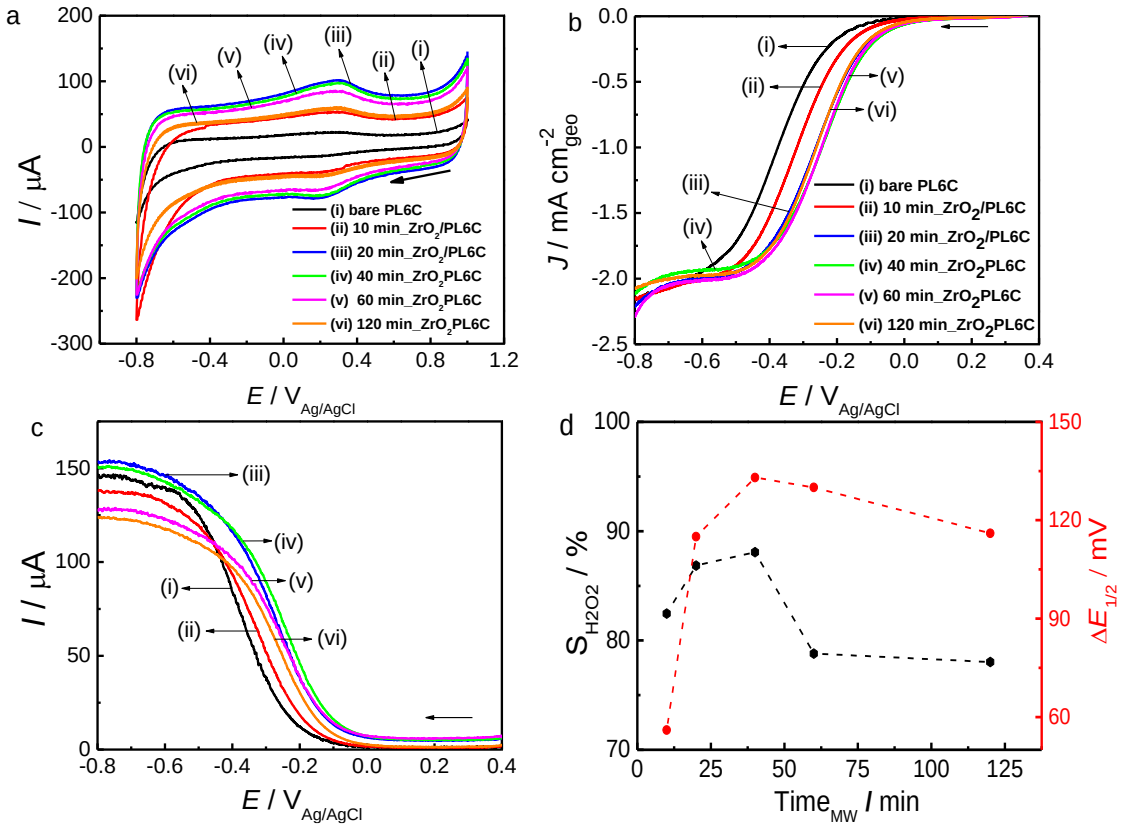

Figure 4. (a) Cyclic voltammograms obtained in N_2-saturated 0.1 mol L^{-1} K_2SO_4, pH=2.5 (H_2SO_4 adjusted), at scan rate of 50 mV s^{-1} and potential window ranging from 1 to -0.8 $V_{Ag/AgCl}$. **(b)** Linear sweep voltammetry in RRDE curves for the disk electrode obtained in O_2-saturated 0.1 mol L^{-1} K_2SO_4, pH=2.5 (H_2SO_4 adjusted), at scan rate of 5 mV^{-1} and potential window ranging from 0.4 to -0.8 V at 900 rpm; **(c)** The values of the currents obtained for the Pt ring electrode during the potential scan on the disk electrode. The ring potential was kept at 1.0 $V_{Ag/AgCl}$. **(d)** Correlation between improvement in the catalytic performance (in terms of $E_{1/2}$), selectivity toward H_2O_2 (S_{H2O2}), and synthesis time.

3.3 Effect of temperature and pressure

After determining the optimal parameter conditions for the initial metallic precursor concentration (fixed at 10 wt.%) and synthesis time (fixed at 40 min), another key parameter was also subjected to analysis - the temperature of synthesis. It is worth noting that variation in synthesis temperature and pressure may lead to conformational changes in the oxide structure, and this may affect the catalytic performance. Thus, the following temperature levels were applied to the Teflon reactor in the microwave oven: 120, 140, and 160 ^oC; these temperature levels corresponded to the following pressure

levels: 2, 4 and 7 bar. The morphological and structural changes in the ZrO_2/PL6C catalyst were monitored by SEM, TEM and XRD techniques, as shown in Fig. 5.

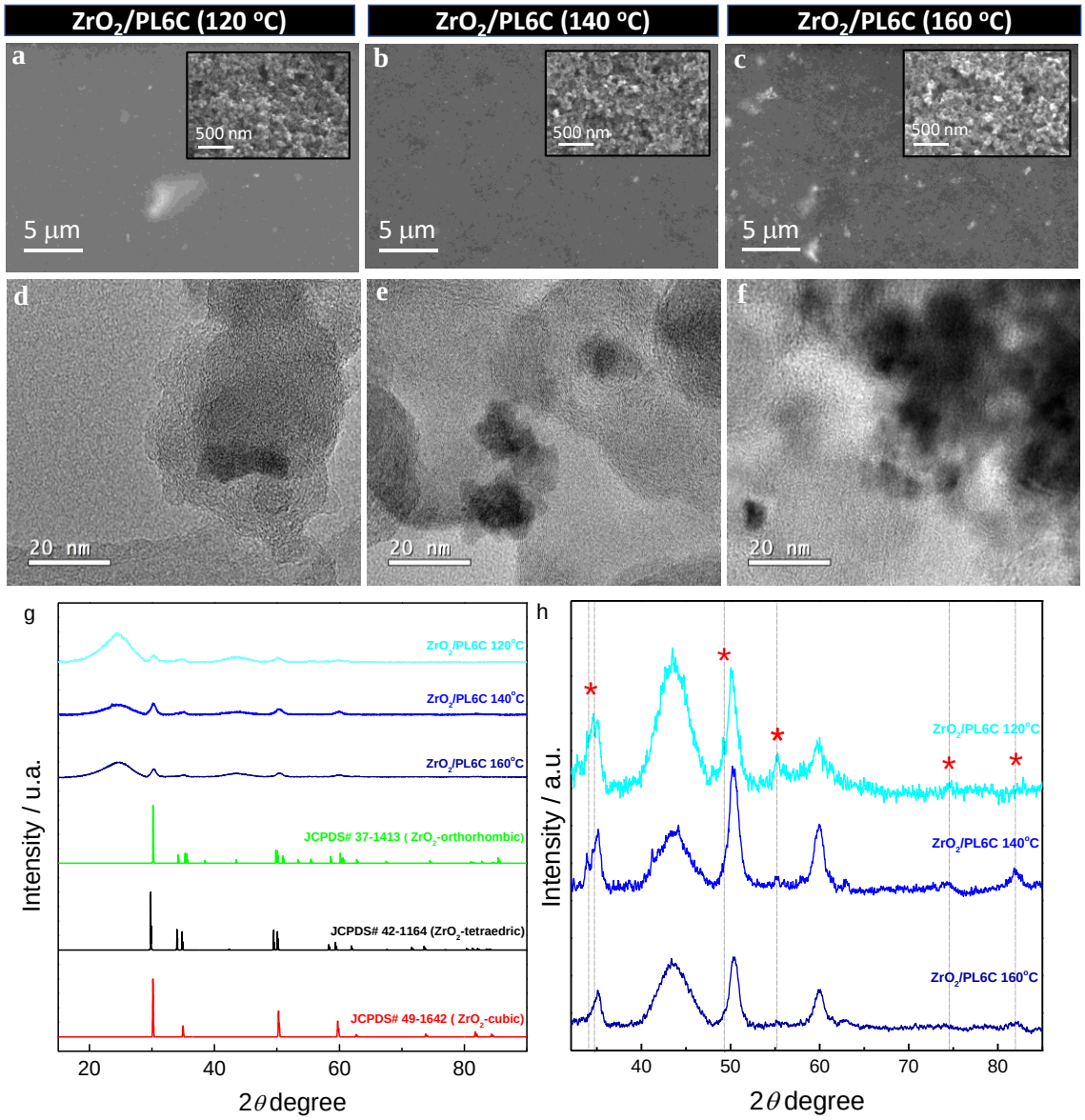

Figure 5. SEM images in (a-c) BSE and SE (inset) mode, (d-f) TEM images, and (g-h) XRD pattern for the ZrO_2/PL6C catalyst produced at different MAH temperatures.

The SEM images (Figs. 5a-c) obtained show that the synthesis temperature plays an influential role on the deposition of the ZrO_2 nanoparticles; this implies that an increase in temperature leads to an increase in both the particle distribution on the PL6C and the size of the particles. The EDX spectra presented in Figure S7 shows that an increase in temperature resulted in higher amounts of crystallized ZrO_2. A further analysis of the

surface morphology by TEM (Figs. 5d-f) showed the presence of large agglomerates of ZrO_2 when the synthesis procedure was conducted above the temperature of 140 °C. The structural analysis of the catalysts by XRD (Figure 5-g) showed the presence of a similar XRD pattern, with a mixture of cubic, orthorhombic, and tetragonal crystalline features for all the ZrO_2/PL6C catalysts. However, a careful look at the diffractograms (c.f. Figure 5h) showed a decrease in intensity of the secondary peaks at 2Θ = 32.4°, 49.2°, 55.2°, 74.5°, and 81.9°, which corresponded to the orthorhombic crystal system, as the synthesis temperature was increased; this shows that the crystallization occurs preferentially in cubic and tetrahedral forms [37,54]. In line with other reports published in the literature [46,53], these findings suggest that the temperature and pressure of the MAH synthesis affect the nucleation-growth process of the metal oxide on the carbon matrix, and this leads to preferential crystallization in certain crystalline systems.

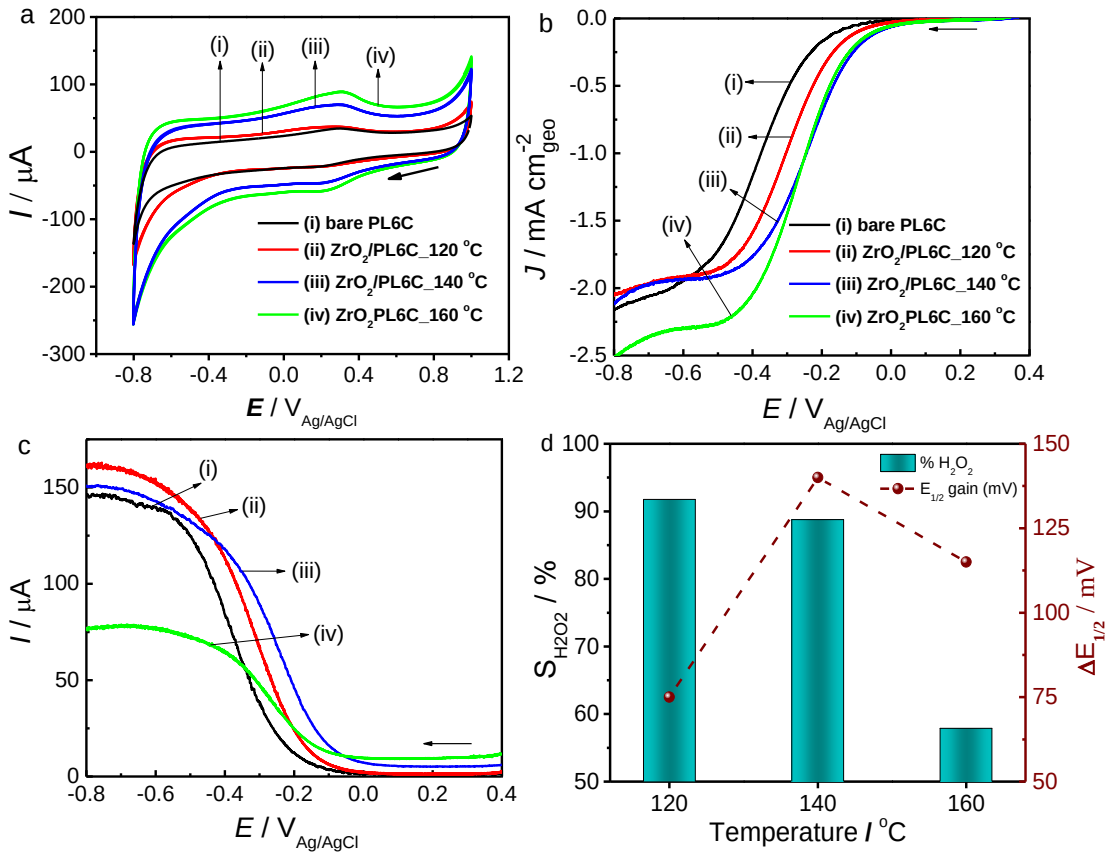

Figure 6. (a) Cyclic voltammograms obtained using N_2-saturated 0.1 mol L^{-1} K_2SO_4, pH=2.5 (H_2SO_4 adjusted), at scan rate of 50 mV s^{-1} and potential window ranging from 1 to -0.8 $V_{Ag/AgCl}$. **(b)** Linear sweep voltammetry in RRDE curves for the disk electrode obtained in O_2-saturated 0.1 mol L^{-1} K_2SO_4, pH=2.5 (H_2SO_4 adjusted) at scan rate of 5 mV^{-1} and potential window ranging from 0.4 to -0.8 V at 900 rpm; **(c)** The values of the currents obtained for the Pt ring electrode during the potential scan on the disk electrode. The ring potential was kept at 1.0 $V_{Ag/AgCl}$. (d) Correlation between the improvement in catalytic performance (in terms of $E_{1/2}$), selectivity toward H_2O_2 (S_{H2O2}), and the temperature applied in the MAH synthesis process.

Figure 6a presents the voltammetric profiles related to the catalysts treated at different MAH temperature levels (and pressure). The ZrO_2/PL6C catalyst produced at 120 ºC exhibited a voltammetric behavior similar to the unmodified PL6C, while the catalysts produced at 140 and 160 ºC presented greater capacitive currents in comparison with the unmodified PCL6; this shows that the use of MAH temperatures above 120º C leads to higher loadings of ZrO_2 on the carbon matrix. These voltammetric responses are in agreement with the results obtained by SEM, TEM and EDX analyses (c.f. Figures 5 and S7).

The electrocatalytic performance in ORR related to the ZrO_2/PL6C catalyst produced at different MAH temperatures are shown in Figures 6b-d. The LSV curves related to the disk electrode (Figure 6b) showed that the ZrO_2/PL6C catalysts produced above the temperature level of 120 ºC exhibited higher ORR activity. However, the ring curves (Figure 6c) showed that the ZrO_2/PL6C produced at 160 ºC exhibited the lowest current for H_2O_2 generation (~75 µA vs 160 µA for the catalyst produced at 120 ºC, and 150 µA for the catalyst produced at 140 ºC). The correlation between the improvement in catalytic performance, the selectivity toward H_2O_2, and the MAH synthesis temperature (Figure 6d) showed that the ZrO_2/PL6C catalyst produced at 140 ºC exhibited the highest ORR activity ($E_{1/2}$ gain of ~140 mV) with selectivity for H_2O_2 production of about 90%.

These findings clearly show that striking a balance between high dispersion of the nanoparticles, surface area, and the loading of the crystallized metal oxide is primarily important if one seeks to improve the ORR catalytic activity of carbon materials via the modification of the materials with ZrO_2.

3.4 Further investigation of the optimized catalyst

To further investigate the physicochemical properties of the optimized ZrO_2/PL6C catalyst produced by the MAH synthesis technique (under the following optimal conditions: 10 wt.% of initial Zr concentration, 40 min of synthesis time, and temperature of 140 ^oC - which presented the best electrocatalytic performance for H_2O_2 generation), the following analyses were conducted: TEM, selected area electron diffraction (SAED), X-ray photoelectron spectroscopy (XPS), and long-term stability test. The high-resolution TEM image obtained for the optimized ZrO_2/PL6C catalyst (Figure 7a) showed that the small ZrO_2 nanoparticles were in direct contact with the PL6C carbon support. The ZrO_2 nanoparticles exhibited lattice fringes measuring 0.29 nm on average; this is typically expected for (1 1 1) diffraction plane in the predominant face-centered cubic structures [52]. Furthermore, the selected area electron diffraction pattern shown in Figure 7b exhibited a polymorphic and low crystallinity profile for the catalyst material due to the high amount of amorphous carbon Printex L6 in the material composition. The electron diffraction pattern presented the diffraction planes (1 1 1), (2 2 0), (2 0 0) and (3 1 1); this can be attributed to the predominance of the cubic phase of ZrO_2 [36,37].

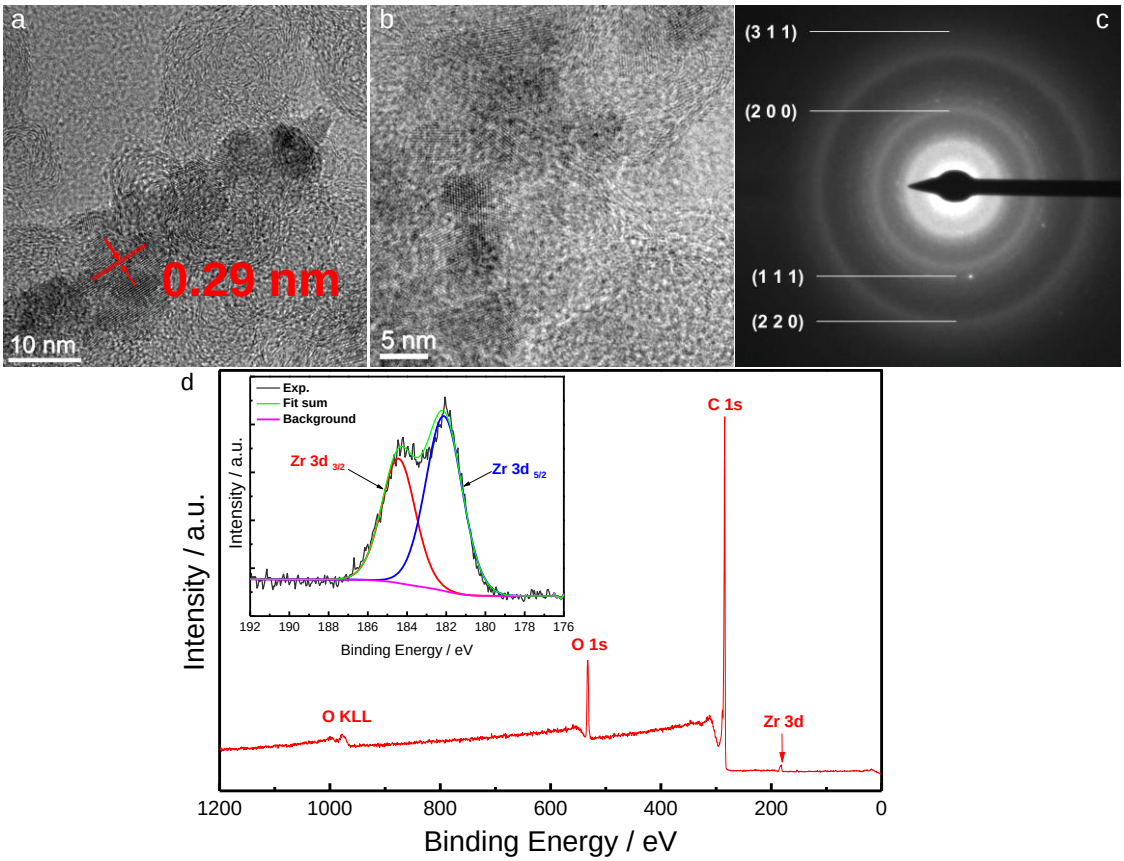

Figure 7. (a,b) HR-TEM images, (c) selected area electron diffraction pattern, and (d) XPS survey spectrum for the optimized ZrO_2/PL6C catalyst. Inset: Narrow XPS spectrum for the Zr 3d region.

XPS analysis was performed aiming at investigating the surface chemistry of the optimized catalyst. The XPS survey spectrum (c. f. Fig. 7d) shows the peaks related to the C1s, O1s, O KLL, and Zr 3d regions, discarding the presence of any contaminant. The XPS narrow spectra for the Zr 3d region (Figure 7d) shows the oxidized form of Zr with the expected spin-orbit splitting ($3d_{3/2}$ and $3d_{5/2}$) and binding energy typically attributed to oxidized Zr species [37,62]. The aforementioned mentioned doublet with binding energies at 184.2 and 181.9 eV show that zirconium is predominantly in its oxidized form - Zr^{4+}, which can be attributed to ZrO_2. It is expected that the oxophilic character of ZrO_2 acts as a driving force for the displacement of electron charges from the PL6C; this may lead to changes in the O_2 adsorption on the carbon surface [32,37,40]. The results obtained

from the XPS analysis demonstrate the efficiency of the microwave assisted hydrothermal synthesis in terms of producing the oxide of interest.

The presence of Zr in its oxidized form (Zr^{4+}) in the catalyst composition indicates that no further oxidation of the metal is possible, and this greatly enhances the electrochemical stability of the catalyst. In order to evaluate the electrochemical long-term stability of the optimized ZrO_2/PL6C catalyst, changes in both ORR activity and H_2O_2 selectivity were monitored before and after the application of 5,000 voltammetric cycles in the potential range of -0.5 to 0.5 $V_{Ag/AgCl}$, at scan rate of 1 V s^{-1}. As can be seen in Figure 8, the LSV curves before and after the long-term stability test for the ZrO_2/PL6C catalyst show that the ORR activity and selectivity toward H_2O_2 production are found to be stable even after the application of 5,000 voltammetric cycles; this evidently points to the high electrochemical stability of the catalyst in acidic condition. Table S2 summarizes the main results obtained for the optimized catalyst ZrO_2/PL6C; which are compared with results previously reported for other catalysts based on metal oxides supported on carbon. It is worth to note that the optimized catalyst as well as the synthesis method proposed here presented advantages with respect to the other catalysts (and their synthesis methods), such as being greenest (uses water as solvent under a lower temperature), produced rapidly, and it demonstrated the highest activity-selectivity combination for the H_2O_2 electrogeneration.

3.5 H_2O_2 electrogeneration using the gas diffusion electrode approach

After the optimization of the synthesis parameters of the catalyst and a rigorous analysis using the RRDE mechanism, a study was conducted aiming at investigating the catalytic activity of the optimized ZrO_2/PL6C catalyst in terms of H_2O_2 generation using the gas diffusion electrode (GDE) approach. Based on the GDE technique, one is able to

evaluate, in a more realistic condition, the catalytic performance of different materials and the impacts of the use of these materials on energy consumption (EC). The gas diffusion electrode technique is regarded more appropriate for real application due to its ability to overcome the limitations imposed by mass transport [8,63,64]. The ability of the GDE to supply oxygen molecules directly to the electrode-solution interface rules out the need for employing O-saturated solution, thus increasing the efficiency of H_2O_2 generation while minimizing the need for electrodes with large surface area [8,63–65]. The GDE cathodes were produced from the following materials: PL6C, ZrO_2/PL6C, and PTFE (provides physical stability to the electrode) (Fig. S9 presents information related to the construction of the GDE). Figure S10 show the profiles related to H_2O_2 electrogeneration evaluated potentiostatically at -0.8, -1.2, -1.6, and -2.0 V. The electrolytic curves for both the PL6C and the ZrO_2/PL6C electrodes exhibited a sharp increase in H_2O_2 concentration in the first 30 min of electrolysis up to the point where an almost constant concentration plateau occurs - this is typically attributed to the presence of electrochemical parasitic reactions [51,66], which mainly consist of further reduction of H_2O_2 on GDE ($H_2O_2 + 2H^+ + 2e^- \rightarrow 2H_2O$) and counter electrode oxidation [6,67]. Over all, both of the GDEs (PL6C and ZrO_2/PL6C) presented significant production of H_2O_2 in the electrolysis at more negative potentials; however, the ZrO_2/PL6C presented greater catalytic activity under all the potentials investigated. For comparison purposes, in the electrolysis performed at -2.0 $V_{Ag/AgCl}$ for 90 min, the ZrO_2/PL6C produced 570 mg L^{-1} of H_2O_2 whereas the unmodified PL6C produced only 250 mg L^{-1}.

To further investigate the kinetics and the energy consumption levels related to the electrogeneration of H_2O_2 for the PL6C and ZrO_2/PL6C electrodes, the kinetic parameters [51,66] and the energy consumption (EC) were estimated and compared (see Table S2). In the electrogeneration of H_2O_2 at -2.0 $V_{Ag/AgCl}$, the carbon-based ZrO_2 catalyst showed

kinetics values ~2 times higher than the bare PL6C catalyst, further providing a decrease of 150 kWh g^{-1} of energy consumption. A detailed discussion on the H_2O_2 electrogeneration using the GDE approach can be found in the Supplementary Information.

4. Conclusion

The present work reported the successful synthesis of electrocatalysts derived from carbon-supported metal oxide for H_2O_2 electrogeneration through the application of a novel, green and fast mechanism based on the microwave-assisted hydrothermal synthesis approach. The loading, dispersion, size, and preferential crystallography of the carbon-modified ZrO_2 nanoparticles was optimized by adjusting the synthesis parameters, such as metal precursor concentration, synthesis time, temperature, and pressure. The results obtained from the RRDE analysis showed that the optimized catalyst produced from ZrO_2-5.1 wt.% on the PL6C electrode support presented a catalytic improvement of 140 mV (in terms of $E_{1/2}$) with respect to ORR and selectivity for H_2O_2 production of 88.8% compared to the unmodified PL6C matrix, which exhibited 78% of H_2O_2 production.

The catalytic improvement in ORR can be attributed to the following factors: 1) the presence of highly dispersed small particles (~7 nm) on the PL6C electrode support; and 2) the increase in *ECSA*, which improved the access to the surface of the catalyst. The presence of ZrO_2 in the modified ZrO_2/PL6C electrode causes a displacement of the electrons from PL6C, and this may lead to changes in the adsorption of O_2 on the carbon surface. Through the application of the GDE assays, the results obtained related to H_2O_2 production helped confirm the superior catalytic performance of the modified ZrO_2/PL6C over the unmodified PL6C. These findings can provide useful insights regarding the

construction of carbon-supported transition metal oxides for future investigations and applications of sustainable catalyst materials for ORR and H_2O_2 electrogeneration.

ASSOCIATED CONTENT

Supporting Information. The supporting information contains figures and tables related to supplementary results and references. This material is available free of charge on the internet at:

Author Contributions

M. S. Kronka: Investigation, Methodology, Validation, Writing - original draft, Writing - review & editing. **P. J. M. Cordeiro-Junior:** Investigation, Methodology, Validation. **L. Mira:** Investigation, Formal analysis. **A. J. dos Santos**: Conceptualization, Writing - review & editing. **G. V. Fortunato**: Validation, Conceptualization, Visualization, Writing - original draft, Writing - review & editing. **M. R. V. Lanza**: Supervision, Funding acquisition, Writing - review & editing. All authors have given their approval for the submission of the final version of the manuscript.

ACKNOWLEDGMENTS

The authors gratefully acknowledge the financial support provided by the following Brazilian research funding agencies: Brazilian National Council for Scientific and Technological Development - CNPq (grant #465571/2014-0, #302874/2017-8 and #427452/2018-0), São Paulo Research Foundation (FAPESP – grants #2014/50945-4, #2017/23464-3, #2016/25831-0, # 2016/19612-4, #2017/10118-0, #2019/20634-0 and #2019/04421-7), and the Coordenação de Aperfeiçoamento de Pessoal de Nível Superior

(CAPES – Finance Code 001). The authors are also grateful to the Laboratory of Structural Characterization (LCE/DEMa/UFSCar) for providing the general facilities used in the conduct of this research.

REFERENCES

[1] R.L. Myers, The 100 Most Important Chemical Compounds: A Reference Guide, CT, Greenwood Press:, Westport, n.d.

[2] J.M. Campos-Martin, G. Blanco-Brieva, J.L.G. Fierro, Hydrogen peroxide synthesis: An outlook beyond the anthraquinone process, Angew. Chemie - Int. Ed. 45 (2006) 6962–6984. doi:10.1002/anie.200503779.

[3] S. Yang, A. Verdaguer-Casadevall, L. Arnarson, L. Silvioli, V. Čolić, R. Frydendal, J. Rossmeisl, I. Chorkendorff, I.E.L. Stephens, Toward the Decentralized Electrochemical Production of H 2 O 2 : A Focus on the Catalysis, ACS Catal. 8 (2018) 4064–4081. doi:10.1021/acscatal.8b00217.

[4] W. Zhou, X. Meng, J. Gao, A.N. Alshawabkeh, Hydrogen peroxide generation from O2 electroreduction for environmental remediation: A state-of-the-art review, Chemosphere. 225 (2019) 588–607. doi:10.1016/j.chemosphere.2019.03.042.

[5] E. Brillas, I. Sirés, M.A. Oturan, Electro-Fenton Process and Related Electrochemical Technologies Based on Fenton's Reaction Chemistry, Chem. Rev. 109 (2009) 6570–6631. doi:10.1021/cr900136g.

[6] S. Yang, A. Verdaguer-Casadevall, L. Arnarson, L. Silvioli, V. Čolić, R. Frydendal, J. Rossmeisl, I. Chorkendorff, I.E.L. Stephens, Toward the Decentralized Electrochemical Production of H2O2 : A Focus on the Catalysis, ACS Catal. 8 (2018) 4064–4081. doi:10.1021/acscatal.8b00217.

[7] S.C. Perry, D. Pangotra, L. Vieira, L.-I. Csepei, V. Sieber, L. Wang, C. Ponce de León, F.C. Walsh, Electrochemical synthesis of hydrogen peroxide from water and oxygen, Nat. Rev. Chem. (2019). doi:10.1038/s41570-019-0110-6.

[8] W. Zhou, X. Meng, J. Gao, A.N. Alshawabkeh, Q. Zhang, M. Zhou, G. Ren, Y.Y. Li, Y.Y. Li, X. Du, Hydrogen peroxide generation from O2 electroreduction for environmental remediation: A state-of-the-art review, Nat. Commun. 225 (2020) 1731. doi:10.1038/s41467-020-15597-y.

[9] E. Yeager, Electrocatalysts for O_2 reduction, Electrochim. Acta. 29 (1984) 1527–1537. doi:10.1016/0013-4686(84)85006-9.

[10] E. Yeager, DIOXYGEN ELECTROCATALYSIS: MECHANISMS IN RELATION TO CATALYST STRUCTURE The 1985 Berzelius Lecture, J. Mol. Catal. 38 (1986) 5–25.

[11] W. Zhou, J. Gao, Y. Ding, H. Zhao, X. Meng, Y. Wang, K. Kou, Y. Xu, S. Wu,

Y. Qin, Drastic enhancement of H2O2 electro-generation by pulsed current for ibuprofen degradation: Strategy based on decoupling study on H2O2 decomposition pathways, Chem. Eng. J. 338 (2018) 709–718. doi:10.1016/j.cej.2017.12.152.

[12] M. Shao, Palladium-based electrocatalysts for hydrogen oxidation and oxygen reduction reactions, J. Power Sources. 196 (2011) 2433–2444. doi:10.1016/j.jpowsour.2010.10.093.

[13] V. Viswanathan, H.A. Hansen, J. Rossmeisl, J.K. Nørskov, Unifying the 2e – and 4e – Reduction of Oxygen on Metal Surfaces, J. Phys. Chem. Lett. 3 (2012) 2948–2951. doi:10.1021/jz301476w.

[14] E. Jung, H. Shin, W. Hooch Antink, Y.-E. Sung, T. Hyeon, Recent Advances in Electrochemical Oxygen Reduction to H 2 O 2 : Catalyst and Cell Design, ACS Energy Lett. 5 (2020) 1881–1892. doi:10.1021/acsenergylett.0c00812.

[15] G.-F. Han, F. Li, W. Zou, M. Karamad, J.-P. Jeon, S.-W. Kim, S.-J. Kim, Y. Bu, Z. Fu, Y. Lu, S. Siahrostami, J.-B. Baek, Building and identifying highly active oxygenated groups in carbon materials for oxygen reduction to H2O2, Nat. Commun. 11 (2020) 2209. doi:10.1038/s41467-020-15782-z.

[16] E. Pizzutilo, O. Kasian, C.H. Choi, S. Cherevko, G.J. Hutchings, K.J.J. Mayrhofer, S.J. Freakley, Electrocatalytic synthesis of hydrogen peroxide on Au-Pd nanoparticles: From fundamentals to continuous production, Chem. Phys. Lett. 683 (2017) 436–442. doi:10.1016/j.cplett.2017.01.071.

[17] J.S. Jirkovský, I. Panas, E. Ahlberg, M. Halasa, S. Romani, D.J. Schiffrin, Single atom hot-spots at Au-Pd nanoalloys for electrocatalytic H 2O 2 production, J. Am. Chem. Soc. 133 (2011) 19432–19441. doi:10.1021/ja206477z.

[18] C.H. Choi, H.C. Kwon, S. Yook, H. Shin, H. Kim, M. Choi, Hydrogen peroxide synthesis via enhanced two-electron oxygen reduction pathway on carbon-coated pt surface, J. Phys. Chem. C. 118 (2014) 30063–30070. doi:10.1021/jp5113894.

[19] A. Verdaguer-casadevall, D. Deiana, M. Karamad, S. Siahrostami, P. Malacrida, T.W. Hansen, J. Rossmeisl, I. Chorkendorff, I.E.L. Stephens, I. Chorkendor, I.E.L. Stephens, Trends in the Electrochemical Synthesis of H 2 O 2 : Enhancing Activity and Selectivity by Electrocatalytic Site Engineering, Nano Lett. 14 (2014) 1603–1608. doi:10.1021/nl500037x.

[20] S. Siahrostami, A. Verdaguer-Casadevall, M. Karamad, D. Deiana, P. Malacrida, B. Wickman, M. Escudero-Escribano, E.A. Paoli, R. Frydendal, T.W. Hansen, I. Chorkendorff, I.E.L. Stephens, J. Rossmeisl, Enabling direct H2O2 production through rational electrocatalyst design, Nat. Mater. 12 (2013) 1137–1143. doi:10.1038/nmat3795.

[21] F. Jaouen, E. Proietti, M. Lefèvre, R. Chenitz, J.-P. Dodelet, G. Wu, H.T. Chung, C.M. Johnston, P. Zelenay, Recent advances in non-precious metal catalysis for oxygen-reduction reaction in polymer electrolyte fuelcells, Energy Environ. Sci. 4 (2011) 114–130. doi:10.1039/C0EE00011F.

[22] S.K. Singh, K. Takeyasu, J. Nakamura, Active Sites and Mechanism of Oxygen Reduction Reaction Electrocatalysis on Nitrogen-Doped Carbon Materials, Adv. Mater. 31 (2019) 1804297. doi:10.1002/adma.201804297.

[23] M.H.M.T. Assumpção, R.F.B. De Souza, D.C. Rascio, J.C.M. Silva, M.L. Calegaro, I. Gaubeur, T.R.L.C. Paixão, P. Hammer, M.R.V. Lanza, M.C. Santos, A comparative study of the electrogeneration of hydrogen peroxide using Vulcan and Printex carbon supports, Carbon N. Y. 49 (2011) 2842–2851. doi:10.1016/j.carbon.2011.03.014.

[24] P.J.M. Cordeiro-Junior, R. Gonçalves, T.T. Guaraldo, R. da Silva Paiva, E.C. Pereira, M.R. de V. Lanza, Oxygen reduction reaction: Semi-empirical quantum mechanical and electrochemical study of Printex L6 carbon black, Carbon N. Y. 156 (2020) 1–9. doi:10.1016/j.carbon.2019.09.036.

[25] F. Sopaj, N. Oturan, J. Pinson, F.I. Podvorica, M.A. Oturan, Effect of cathode material on electro-Fenton process efficiency for electrocatalytic mineralization of the antibiotic sulfamethazine, Chem. Eng. J. 384 (2020) 123249. doi:10.1016/j.cej.2019.123249.

[26] A. Moraes, M.H.M.T. Assumpção, F.C. Simões, V.S. Antonin, M.R.V. Lanza, P. Hammer, M.C. Santos, Surface and Catalytical effects on Treated Carbon Materials for Hydrogen Peroxide Electrogeneration, Electrocatalysis. 7 (2016) 60–69. doi:10.1007/s12678-015-0279-5.

[27] Q. Zhang, M. Zhou, G. Ren, Y.Y. Li, Y.Y. Li, X. Du, Highly efficient electrosynthesis of hydrogen peroxide on a superhydrophobic three-phase interface by natural air diffusion, Nat. Commun. 11 (2020) 1731. doi:10.1038/s41467-020-15597-y.

[28] M. Ledendecker, E. Pizzutilo, G. Malta, G. V Fortunato, K.J.J. Mayrhofer, G.J. Hutchings, S.J. Freakley, Isolated Pd Sites as Selective Catalysts for Electrochemical and Direct Hydrogen Peroxide Synthesis, ACS Catal. (2020) 5928–5938. doi:10.1021/acscatal.0c01305.

[29] G. V. Fortunato, M.S. Kronka, A.J. dos Santos, M. Ledendecker, M.R.V. Lanza, Low Pd loadings onto Printex L6: Synthesis, characterization and performance towards H2O2 generation for electrochemical water treatment technologies, Chemosphere. 259 (2020) 127523. doi:10.1016/j.chemosphere.2020.127523.

[30] M.S. Kronka, F.L. Silva, A.S. Martins, M.O. Almeida, K.M. Honório, M.R. V. Lanza, Tailoring the ORR selectivity for H 2 O 2 electrogeneration by modification of Printex L6 carbon with 1,4-naphthoquinone: a theoretical, experimental and environmental application study , Mater. Adv. (2020) 1318–1329. doi:10.1039/d0ma00290a.

[31] R.B. Valim, R.M. Reis, P.S. Castro, A.S. Lima, R.S. Rocha, M. Bertotti, M.R. V Lanza, Electrogeneration of hydrogen peroxide in gas diffusion electrodes modified with tert-butyl-anthraquinone on carbon black support, Carbon N. Y. 61 (2013) 236–244. doi:10.1016/j.carbon.2013.04.100.

[32] J.F. Carneiro, M.J. Paulo, M. Siaj, A.C. Tavares, M.R.V. Lanza, Nb2O5 nanoparticles supported on reduced graphene oxide sheets as electrocatalyst for the H2O2 electrogeneration, J. Catal. 332 (2015) 51–61. doi:10.1016/j.jcat.2015.08.027.

[33] G. Ren, M. Zhou, Q. Zhang, X. Xu, Y. Li, P. Su, A novel stacked flow-through electro-Fenton reactor as decentralized system for the simultaneous removal of

pollutants (COD, NH3-N and TP) and disinfection from domestic sewage containing chloride ions, Chem. Eng. J. 387 (2020) 124037. doi:10.1016/j.cej.2020.124037.

[34] C. Xia, Y. Xia, P. Zhu, L. Fan, H. Wang, Direct electrosynthesis of pure aqueous H 2 O 2 solutions up to 20% by weight using a solid electrolyte, Science (80-.). 366 (2019) 226–231. doi:10.1126/science.aay1844.

[35] K.-H. Wu, D. Wang, X. Lu, X. Zhang, Z. Xie, Y. Liu, B.-J. Su, J.-M. Chen, D.-S. Su, W. Qi, S. Guo, Highly Selective Hydrogen Peroxide Electrosynthesis on Carbon: In Situ Interface Engineering with Surfactants, Chem. 6 (2020) 1443–1458. doi:10.1016/j.chempr.2020.04.002.

[36] J.F. Carneiro, M.J. Paulo, M. Siaj, A.C. Tavares, M.R. V Lanza, Zirconia on Reduced Graphene Oxide Sheets: Synergistic Catalyst with High Selectivity for H2O2 Electrogeneration, ChemElectroChem. 4 (2017) 508–513. doi:10.1002/celc.201600760.

[37] J.F. Carneiro, L.C. Trevelin, A.S. Lima, G.N. Meloni, M. Bertotti, P. Hammer, R. Bertazzoli, M.R.V. Lanza, Synthesis and Characterization of ZrO2/C as Electrocatalyst for Oxygen Reduction to H2O2, Electrocatalysis. 8 (2017) 189–195. doi:10.1007/s12678-017-0355-0.

[38] H. Li, P. Wen, Q. Li, C. Dun, J. Xing, C. Lu, S. Adhikari, L. Jiang, D.L. Carroll, S.M. Geyer, Earth-Abundant Iron Diboride (FeB2) Nanoparticles as Highly Active Bifunctional Electrocatalysts for Overall Water Splitting, Adv. Energy Mater. 7 (2017) 1–12. doi:10.1002/aenm.201700513.

[39] Y. Li, J. Han, B. Xie, Y. Li, S. Zhan, Y. Tian, Synergistic degradation of antimicrobial agent ciprofloxacin in water by using 3D CeO2/RGO composite as cathode in electro-Fenton system, J. Electroanal. Chem. 784 (2017) 6–12. doi:10.1016/j.jelechem.2016.11.057.

[40] F. Xu, T. Song, Y. Xu, Y. Chen, S. Zhu, S. Shen, A new cathode using CeO2/MWNT for hydrogen peroxide synthesis through a fuel cell, J. Rare Earths. 27 (2009) 128–133. doi:10.1016/S1002-0721(08)60206-9.

[41] M.H.M.T. Assumpção, A. Moraes, R.F.B. De Souza, M.L. Calegaro, M.R.V. Lanza, E.R. Leite, M.A.L. Cordeiro, P. Hammer, M.C. Santos, Influence of the preparation method and the support on H2O2 electrogeneration using cerium oxide nanoparticles, Electrochim. Acta. 111 (2013) 339–343. doi:10.1016/j.electacta.2013.07.187.

[42] P.S. Simas, V.S. Antonin, L.S. Parreira, P. Hammer, F.L. Silva, M.S. Kronka, R.B. Valim, M.R.V. Lanza, M.C. Santos, Carbon Modified with Vanadium Nanoparticles for Hydrogen Peroxide Electrogeneration, Electrocatalysis. 8 (2017) 311–320. doi:10.1007/s12678-017-0366-x.

[43] J. Jouhannaud, J. Rossignol, D. Stuerga, Rapid synthesis of tin (IV) oxide nanoparticles by microwave induced thermohydrolysis, J. Solid State Chem. 181 (2008) 1439–1444. doi:10.1016/j.jssc.2008.02.040.

[44] B. Zheng, J. Wang, F. Bin Wang, X.H. Xia, Synthesis of nitrogen doped graphene with high electrocatalytic activity toward oxygen reduction reaction, Electrochem. Commun. 28 (2013) 24–26. doi:10.1016/j.elecom.2012.11.037.

[45] Z. Liu, L.M. Gan, L. Hong, W. Chen, J.Y. Lee, Carbon-supported Pt nanoparticles as catalysts for proton exchange membrane fuel cells, J. Power Sources. 139 (2005) 73–78. doi:10.1016/j.jpowsour.2004.07.012.

[46] M.L. Moreira, J. Andrés, J.A. Varela, E. Longo, Synthesis of Fine Micro-sized BaZrO 3 Powders Based on a Decaoctahedron Shape by the Microwave-Assisted Hydrothermal Method , Cryst. Growth Des. 9 (2008) 833–839. doi:10.1021/cg800433h.

[47] J. Huang, C. Xia, L. Cao, X. Zeng, Facile microwave hydrothermal synthesis of zinc oxide one-dimensional nanostructure with three-dimensional morphology, Mater. Sci. Eng. B Solid-State Mater. Adv. Technol. 150 (2008) 187–193. doi:10.1016/j.mseb.2008.05.014.

[48] R. Schmidt, J.P. Gonjal, E. Morán, Microwaves: Microwave-Assisted Hydrothermal Synthesis of Nanoparticles, CRC Concise Encycl. Nanotechnol. 12 (2018) 561–570. doi:10.1201/b19457-49.

[49] K.S. Egorova, V.P. Ananikov, Toxicity of Metal Compounds: Knowledge and Myths, Organometallics. 36 (2017) 4071–4090. doi:10.1021/acs.organomet.7b00605.

[50] C.C.L. McCrory, S. Jung, J.C. Peters, T.F. Jaramillo, Benchmarking Heterogeneous Electrocatalysts for the Oxygen Evolution Reaction, J. Am. Chem. Soc. 135 (2013) 16977–16987. doi:10.1021/ja407115p.

[51] F.L. Silva, R.M. Reis, W.R.P. Barros, R.S. Rocha, M.R.V. Lanza, Electrogeneration of hydrogen peroxide in gas diffusion electrodes: Application of iron (II) phthalocyanine as a modifier of carbon black, J. Electroanal. Chem. 722–723 (2014) 32–37. doi:10.1016/j.jelechem.2014.03.007.

[52] J. Moreira, V. Bocalon Lima, L. Athie Goulart, M.R.V. Lanza, Electrosynthesis of hydrogen peroxide using modified gas diffusion electrodes (MGDE) for environmental applications: Quinones and azo compounds employed as redox modifiers, Appl. Catal. B Environ. 248 (2019) 95–107. doi:10.1016/j.apcatb.2019.01.071.

[53] S.C. Padmanabhan, T.W. Collins, S.C. Pillai, D.E. McCormack, J.M. Kelly, J.D. Holmes, M.A. Morris, A conceptual change in crystallisation mechanisms of oxide materials from solutions in closed systems, Sci. Rep. 10 (2020) 18414. doi:10.1038/s41598-020-75241-z.

[54] Z. Azdad, L. Marot, L. Moser, R. Steiner, E. Meyer, Valence band behaviour of zirconium oxide, Photoelectron and Auger spectroscopy study, Sci. Rep. 8 (2018) 1–6. doi:10.1038/s41598-018-34570-w.

[55] L. Zhang, A.A.S. Gonçalves, M. Jaroniec, Identification of preferentially exposed crystal facets by X-ray diffraction, RSC Adv. 10 (2020) 5585–5589. doi:10.1039/D0RA00769B.

[56] Y. Liang, Y. Li, H. Wang, J. Zhou, J. Wang, T. Regier, H. Dai, Co3O4 nanocrystals on graphene as a synergistic catalyst for oxygen reduction reaction, Nat. Mater. 10 (2011) 780–786. doi:10.1038/nmat3087.

[57] A. Sarapuu, K. Vaik, D.J. Schiffrin, K. Tammeveski, Electrochemical reduction

of oxygen on anodically pre-treated and chemically grafted glassy carbon electrodes in alkaline solutions, J. Electroanal. Chem. 541 (2003) 23–29. doi:10.1016/j.elecom.2003.10.003.

[58] K. Tammeveski, K. Kontturi, R.J. Nichols, R.J. Potter, D.J. Schiffrin, Surface redox catalysis for O2 reduction on quinone-modified glassy carbon electrodes, J. Electroanal. Chem. 515 (2001) 101–112. doi:https://doi.org/10.1016/S0022-0728(01)00633-7.

[59] U.A. Paulus, T.J. Schmidt, H.A. Gasteiger, R.J. Behm, Oxygen reduction on a high-surface area Pt/Vulcan carbon catalyst: a thin-film rotating ring-disk electrode study, J. Electroanal. Chem. 495 (2001) 134–145. doi:10.1016/S0022-0728(00)00407-1.

[60] G. Chen, M.B. Stevens, Y. Liu, L.A. King, J. Park, T.R. Kim, R. Sinclair, T.F. Jaramillo, Z. Bao, Nanosized Zirconium Porphyrinic Metal–Organic Frameworks that Catalyze the Oxygen Reduction Reaction in Acid, Small Methods. 4 (2020) 2000085. doi:10.1002/smtd.202000085.

[61] K.P. Kepp, A Quantitative Scale of Oxophilicity and Thiophilicity, Inorg. Chem. 55 (2016) 9461–9470. doi:10.1021/acs.inorgchem.6b01702.

[62] B. Rungtaweevoranit, J. Baek, J.R. Araujo, B.S. Archanjo, K.M. Choi, O.M. Yaghi, G.A. Somorjai, Copper Nanocrystals Encapsulated in Zr-based Metal-Organic Frameworks for Highly Selective CO2 Hydrogenation to Methanol, Nano Lett. 16 (2016) 7645–7649. doi:10.1021/acs.nanolett.6b03637.

[63] R.M. Reis, A.A.G.F. Beati, R.S. Rocha, M.H.M.T. Assumpção, M.C. Santos, R. Bertazzoli, M.R. V Lanza, Use of gas diffusion electrode for the in situ generation of hydrogen peroxide in an electrochemical flow-by reactor, Ind. Eng. Chem. Res. 51 (2012) 649–654. doi:10.1021/ie201317u.

[64] J.F. Carneiro, R.S. Rocha, P. Hammer, R. Bertazzoli, M.R.V. Lanza, Hydrogen peroxide electrogeneration in gas diffusion electrode nanostructured with Ta2O5, Appl. Catal. A Gen. 517 (2016) 161–167. doi:10.1016/j.apcata.2016.03.013.

[65] T. Muddemann, D.R. Haupt, M. Sievers, U. Kunz, Improved Operating Parameters for Hydrogen Peroxide-Generating Gas Diffusion Electrodes, Chemie Ing. Tech. 92 (2020) 505–512. doi:10.1002/cite.201900137.

[66] W.R.P. Barros, R.M. Reis, R.S. Rocha, M.R.V. Lanza, Electrogeneration of hydrogen peroxide in acidic medium using gas diffusion electrodes modified with cobalt (II) phthalocyanine, Electrochim. Acta. 104 (2013) 12–18. doi:10.1016/j.electacta.2013.04.079.

[67] A.J. dos Santos, S. Garcia-Segura, S. Dosta, I.G. Cano, C.A. Martínez-Huitle, E. Brillas, A ceramic electrode of ZrO2-Y2O3 for the generation of oxidant species in anodic oxidation. Assessment of the treatment of Acid Blue 29 dye in sulfate and chloride media, Sep. Purif. Technol. 228 (2019) 115747. doi:10.1016/j.seppur.2019.115747.

Graphical Abstract

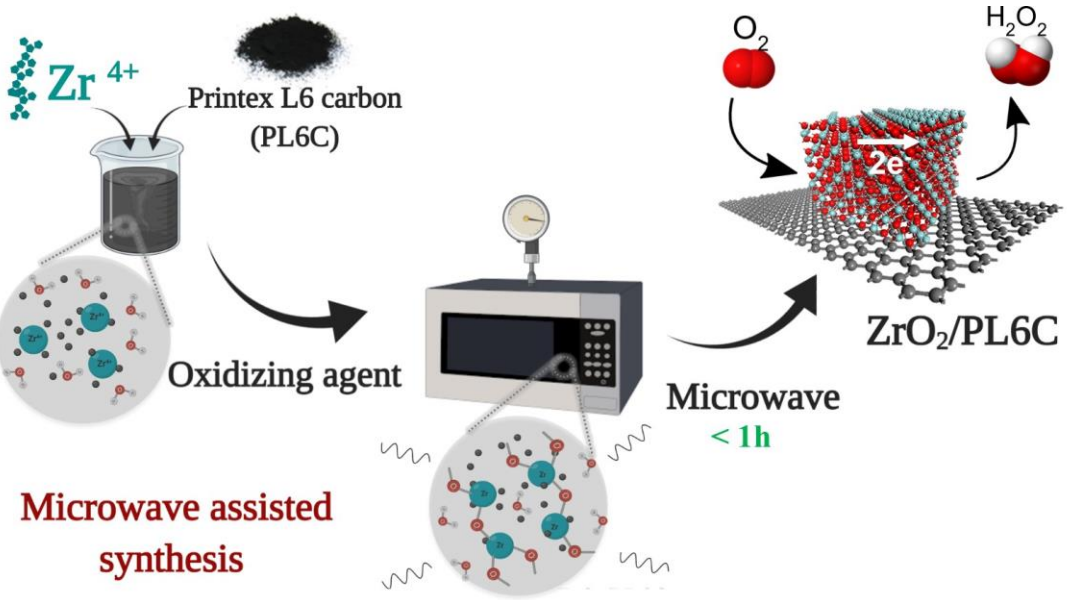

Highlights

- Carbon-based metal oxide catalyst was produced by sustainable MAH approach.
- ZrO_2-5.1 wt.% on PL6C presented a gain of 140 mV in $E_{1/2}$ and S_{H2O2} of 88.8 %.
- Particles dispersion, *ECSA*, and oxide loading are key elements to consider in ORR.
- ZrO_2/PL6C presented k_{app} values for H_2O_2 production ~2x higher than bare PL6C.